INTERNATIONAL JOURNAL FOR NUMERICAL METHODS IN FLUIDS, VOL. 24, 185–214 (1997)

# AN IMPROVED MAC METHOD (SIMAC) FOR UNSTEADY HIGH-REYNOLDS FREE SURFACE FLOWS

VINCENZO ARMENIO

*Department of Naval Architecture, Ocean and Environmental Engineering, University of Trieste, Via Valerio 10, I-34127 Trieste, Italy*

## SUMMARY

A modified MAC method (SIMAC; semi-implicit marker and cell) is proposed which accurately treats unsteady high-Reynolds free surface problems. SIMAC solves the Navier–Stokes equations in primitive variables on a non-uniform staggered Cartesian grid by means of a finite difference scheme. The convective term is treated explicitly by employing a second-order upwind scheme in space (HLPA) and the Adams–Bashforth technique in time. The diffusive part is solved by means of the implicit approximate factorization technique. A multigrid technique based on the additive correction strategy is employed to solve the Poisson equation for the pressure. Finally, the free surface treatment is carried out using massless particles which divide the domain of integration into full and empty cells as in a standard MAC method.

The algorithm is used for the analysis of large-amplitude water sloshing in retangular unbaffled and baffled containers. Experimental tests have been carried out in order to validate the algorithm. Numerical results satisfactorily agree with experimental data for the whole range of filing conditions analysed here.

KEY WORDS: viscous free surface flows; approximate factorization; multigrid technique; water sloshing; experimental validation

## 1. INTRODUCTION

Most problems in ship hydrodynamics are characterized by unsteady flows in the presence of a free surface and are affected by the water viscosity. Typical problems in this area are the large-amplitude sloshing of liquids in baffled tanks and the hydrodynamic interaction between water waves and oscillating free surface-piercing bodies.

Several techniques have already been developed to treat such problems. The MAC method of Welch *et al.*[1] represents the first attempt to simulate unsteady viscous flows with a free surface. It solves the unsteady primitive variables Navier–Stokes equations on uniform Cartesian staggered grids. The velocity field is predicted using an explicit second-order centred discretization of the convective and diffusive terms.

The continuity equation, written as a Poisson equation for the pressure, is solved with a point-by-point procedure and the Lagrangian movement of the free surface is identified by massless particles (markers). The domain of integration of the governing equations is fixed in time, the liquid portion being identified by the flagging of the cells depending on their own position compared with the instantaneous position of the markers.

The method was then improved. At first efforts were devoted to a better calculation of the pressure at the free surface,[2–4] then to a more accurate tracking of the free surface itself.

CCC 0271–2091/97/020185–30

*Received 1 July 1994*
*Revised 1 May 1996*

SUMMAC,[2] SOLA-VOF[5] and TUMMAC[6–9] are typical examples of modified MAC methods. However, these algorithms share common features:

(a) the subdivision of the computational domain in full, free surface and empty cells
(b) the solution of a Poisson equation for the pressure
(c) the explicit updating of the velocity field.

Mainly owing to the diffusive constraint on the time step, the explicit updating of the velocity field does not allow the accurate solution of the viscous stress at the solid boundaries, even if non-uniform grids are employed.

For the reasons previously outlined, in the past the MAC method was applied to the computation of very viscous flows with interfaces or to problems in which the viscous stress can be neglected. Basically, this is due to the fact that the nature of the algorithm requires the use of coarse grids.

Over the last few years a number of very promising techniques have been developed which solve the governing equations in generalized co-ordinates within a time dependent domain of integration.[10,11] Despite the great accuracy of these methods, they require a large amount of CPU time and their effectiveness in handling highly distorted free surface patterns has yet to be proved.

Recently the need has emerged to find a powerful technique which allows the solution of the liquid sloshing problem in ship tanks. Indeed, in a recent paper,[12] discrepancies between numerical results and experimental data have been ascribed to the artificial dissipation due to grid coarseness. As a conclusion the author points out the need for an accelerating technique which can contribute to the accurate solution of the viscous stress at the solid boundaries and allows for the inclusion of a turbulence model.

The present paper seeks to provide a contribution to the solution of the problem. The main idea is based on a modification of the MAC method which updates the velocity field by means of the well established semi-implicit technique. The viscous stress is solved implicitly by means of the approximate factorization technique and the convective part is treated explicitly by using the Adams–Bashforth time advancement technique. The semi-implicit treatment makes it possible to overcome the constraint on the time steps related to the diffusive condition for the stability and at the same time to use high-order wiggle-free schemes for the convective part. The resulting algorithm is formally second order accurate in both space and time.

It is well known that in viscous unsteady computations a large CPU time is needed for the solution of the pressure equation in order to achieve a free divergence velocity field at each time step. For this reason it is crucial to accelerate the convergence of the pressure equation. In the present paper this

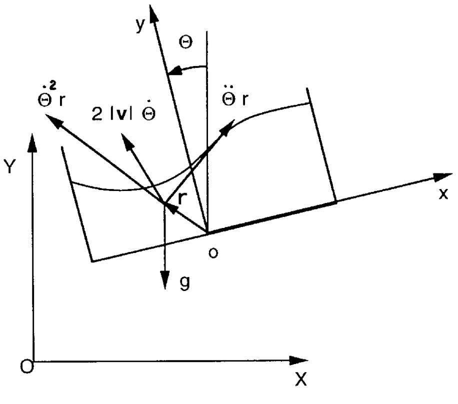

Figure 1. Frame of references used in computations and representation of body forces per unit volume acting throughout liquid

objective has been achieved by using the additive correction multigrid technique, thanks to which the algorithm was accelerated by a factor of seven to nine as compared with the solution obtained with an SOR procedure.

The algorithm, called SIMAC (semi-implicit marker and cell), can handle very stretched grids and allows for high-Reynolds-number computations.

## 2. GOVERNING EQUATIONS

In a frame of reference fixed to the body (Figure 1) the two-dimensional Navier–Stokes equations for an incompressible flow written in primitive variables are:

$$\frac{\partial u}{\partial x}+\frac{\partial v}{\partial y}=0, \tag{1}$$

$$\frac{\partial u}{\partial t}+\frac{\partial u^2}{\partial x}+\frac{\partial uv}{\partial y}+\frac{\partial P}{\partial x}=\nu\left(\frac{\partial^2 u}{\partial x^2}+\frac{\partial^2 u}{\partial y^2}\right)+B_x, \tag{2}$$

$$\frac{\partial v}{\partial t}+\frac{\partial uv}{\partial x}+\frac{\partial v^2}{\partial y}+\frac{\partial P}{\partial y}=\nu\left(\frac{\partial^2 v}{\partial x^2}+\frac{\partial^2 v}{\partial y^2}\right)+B_y, \tag{3}$$

where $u$ and $v$ are the velocity components referred to the above-mentioned frame of reference, $P=(p-p_{\mathrm{atm}})/\rho$ is the relative pressure, $\nu$ is the kinematic viscosity and $B_x$ and $B_y$ are the components of the body forces acting throughout the liquid. The origin of the frame of reference is located at the centre of the tank bottom.

In the present work SIMAC is applied to the solution of an internal flow problem (liquid sloshing in rectangular containers). In this case the following set of conditions should be considered at the boundaries of the domain.

### *Rigid walls*

The normal and tangential components of the velocity are zero.

### *Free surface*

Kinematic and dynamic boundary conditions have to be applied at the free surface. In particular the following non-linear kinematic condition, able to deal with large-amplitude non-overturning waves, should be used:

$$\frac{\partial \eta}{\partial t}+u\frac{\partial \eta}{\partial x}-v=0, \tag{4}$$

where $\eta(x,t)$ is the height of the free surface above the tank bottom.

Several dynamic conditions could be taken into account at the free surface depending on the degree of accuracy required.

In particular the stress normal to the free surface must counterbalance the external applied forces and the stress tangential to the free surface must disappear.

If one neglects the surface tension related to the free surface local curvature, the above conditions can be written as

$$P = \frac{2\nu}{1 + \partial\eta^2/\partial x}\left[\frac{\partial\eta^2}{\partial x}\frac{\partial u}{\partial x} - \frac{\partial\eta}{\partial x}\left(\frac{\partial u}{\partial y} + \frac{\partial v}{\partial x}\right) + \frac{\partial v}{\partial y}\right], \tag{5}$$

$$2\frac{\partial\eta}{\partial x}\frac{\partial u}{\partial x} + \left(\frac{\partial\eta^2}{\partial x} - 1\right)\left(\frac{\partial u}{\partial y} + \frac{\partial v}{\partial x}\right) - 2\frac{\partial\eta}{\partial x}\frac{\partial v}{\partial y} = 0. \tag{6}$$

Owing to the difficulties encountered by the MAC method in accurately solving the boundary layer at the free surface,[8] in the present work equation (6) is neglected and equation (5) is simplified as

$$P = 0 \quad \text{on } y = \eta(x, t). \tag{7}$$

## 3. COMPUTATIONAL METHOD

The algorithm proposed in this work is basically a MAC method. It follows that the governing equations are solved by means of a fractional step or time-splitting technique. In the first stage a velocity field satisfying the momentum equations is calculated; in the second step this field is corrected to a free divergence one by means of a scalar operator $\Phi$. This allows us to write the continuity equation as a Poisson equation for $\Phi$.

As already mentioned, the family of MAC methods treats the convective and diffusive terms explicitly. The order of space discretization basically depends on the scheme used for the convective term. If hybrid schemes are employed,[6] the algorithm is first-order-accurate. If, instead, one uses third-order upwinding[9] or second-order centred schemes in conjunction with fourth-order artificial dissipation, the algorithm is high-order.

The explicit treatment of the diffusive term involves a severe restriction of the time step available for low-Reynolds-number flows and near the boundaries when stretched meshes are used. The latter case makes the calculation unfeasible in hydrodynamics.

On the other hand a fully implicit scheme entails the inversion of a sparse matrix if high-order schemes are employed for the discretization of the convective terms.

Thus a semi-implicit treatment can eliminate the restrictions related to the use of the explicit differencing of the diffusive term and at the same time allows the use of high-order schemes for the convective part. The latter is a particularly favourable circumstance when large Peclet numbers are expected during the computation.

### *3.1. Fractional step formulation*

Several formulations of semi-implicit, fractional step algorithms have been developed in the past. In 1990 Gresho[13] clarified the theoretical background that makes it possible to solve the Navier–Stokes equations via a semi-implicit projection method. In his contribution he paid special attention to the treatment of the intermediate boundary conditions.

Three semi-implicit formulations will be briefly described hereafter.

Kim and Moin,[14] after disregarding the pressure terms in the momentum equation, solved the set of equations:

$$\frac{\hat{\mathbf{u}} - \mathbf{u}^n}{\Delta t} = -\tfrac{1}{2}[3\ \mathrm{Conv}(\mathbf{u})^n - \mathrm{Conv}(\mathbf{u})^{n-1}] + \tfrac{1}{2}\nu\nabla^2(\hat{\mathbf{u}} + \mathbf{u}^n), \tag{8}$$

$$\frac{\mathbf{u}^{n+1} - \hat{\mathbf{u}}}{\Delta t} = -\nabla\Phi^{n+1}, \tag{9}$$

where $\Phi$ is a computational pressure projecting the velocity field in a free divergence field.

If one takes the divergence of (9) and considers that the updated velocity field must satisfy the continuity equation, it follows that

$$\nabla^2\Phi^{n+1} = \frac{1}{\Delta t}\nabla\hat{\mathbf{u}}. \tag{10}$$

Kim and Moin have shown that the computational scheme is consistent provided that the following condition is satisfied at the boundaries $\Gamma$:

$$\hat{\mathbf{u}}_\Gamma = \mathbf{u}_\Gamma^{n+1} + \Delta t\frac{\partial\Phi}{\partial n}. \tag{11}$$

It should to be noticed that the physical pressure is given by the second-order approximation

$$P^{n+1} = \Phi^{n+1} + \frac{\nu\Delta t}{2}\nabla^2\Phi^{n+1}. \tag{12}$$

Later on Esposito[15] proved that a consistent scheme can be achieved by explicitly introducing the physical pressure in equation (8) and imposing the simplified boundary condition

$$\hat{\mathbf{u}}_\Gamma = \mathbf{u}_\Gamma^{n+1}, \tag{13}$$

which makes it possible to use the homogeneous boundary condition $\partial\Phi/\partial n = 0$ in equation (10).

In this scheme the physical pressure is related to the operator $\Phi$ by the equation

$$P^{n+1} = P^n + \Phi^{n+1} + \frac{\nu\Delta t}{2}\nabla^2\Phi^{n+1}. \tag{14}$$

Finally Huser and Biringen[16] showed that it is possible to use only the operator $\Phi$ and at the same time to apply equation (13), which results in the use of the homogeneous boundary conditions $\partial\Phi/\partial n = 0$.

In order to avoid the difficulties which can arise in a free surface problem when operating with two different scalar functions, $P$ and $\Phi$ respectively, the model by Huser and Biringen was used.

The two step advancement of the solution is performed as follows:

$$\frac{\hat{\mathbf{u}} - \mathbf{u}^n}{\Delta t} = -\tfrac{1}{2}[3\ \mathrm{Conv}(\mathbf{u})^n - \mathrm{Conv}(\mathbf{u})^{n-1}] + \tfrac{1}{2}\nu\nabla^2(\hat{\mathbf{u}} + \mathbf{u}^n) - \nabla\Phi^n + \mathbf{B}^n, \tag{15}$$

$$\frac{\mathbf{u}^{n+1} - \hat{\mathbf{u}}}{\Delta t} = -(\nabla\Phi^{n+1} - \nabla\Phi^n). \tag{16}$$

If one takes the divergence of equation (16) and rearranges it, the result will be

$$\nabla^2\Phi^{n+1} = \frac{1}{\Delta t}\nabla\hat{\mathbf{u}} + \nabla^2\Phi^n. \tag{17}$$

It has been shown[16] that the use of homogeneous boundary conditions ($\partial\Phi/\partial n = 0$) deriving from the use of equation (13) provides for a consistent second-order scheme. Finally the pressure $P$ is given by the second-order approximation

$$P^{n+1} = \Phi^{n+1} + \frac{\nu\Delta t}{2}(\nabla^2\Phi^{n+1} - \nabla^2\Phi^n). \tag{18}$$

### 3.2. Convective terms

In this work several schemes were tested. In short it can be said that the second-order centred scheme or the third-order unbounded upwind scheme (QUICK) needs the introduction of the fourth-order artificial dissipative term. Nevertheless, great difficulties were encountered in choosing the artificial viscosity coefficient conveniently. In the tests performed it was observed that the use of the second-order bounded scheme (HLPA)[17] ensures a wiggle-free solution without any significant loss of accuracy even for large Peclet (Reynolds cell) numbers.

### 3.3. Diffusive terms

The diffusive terms are treated implicitly by means of the Crank–Nicolson scheme using the approximate factorization technique.

Starting from equation (15), the intermediate velocity field is calculated in two different steps, each of them involving one direction.

Equation (15) in vectorial notation can be rewritten as:

$$(1 - A_1 - A_2)(\hat{\mathbf{u}} - \mathbf{u}^n) = -\Delta t\nabla\Phi^n - \frac{\Delta t}{2}[3\,\mathrm{Conv}(\mathbf{u})^n - \mathrm{Conv}(\mathbf{u})^{n-1}] + 2(A_1 + A_2)\mathbf{u}^n + \mathbf{B}^n, \tag{19}$$

where $A_1 = \nu(\Delta t/2)(\partial^2/\partial x^2)$ and $A_2 = \nu(\Delta t/2)(\partial^2/\partial y^2)$.

The LHS of (19) is then manipulated as

$$1 - A_1 - A_2 \approx (1 - A_1)(1 - A_2), \tag{20}$$

with the introduction of the extra term $A_1A_2$ proportional to $\Delta t^2$.

At each time step a two-stage algorithm is implemented as follows. First the following set of equations is solved in the $x$-direction:

$$(1 - A_1)\Delta\mathbf{u}^* = -\Delta t\nabla(\Phi^n) - \frac{\Delta t}{2}[3\,\mathrm{Conv}(\mathbf{u})^n - \mathrm{Conv}(\mathbf{u})^{n-1}] + 2(A_1 + A_2)\mathbf{u}^n + \mathbf{B}^n. \tag{21}$$

Then at the second stage the following set of equations is solved in the $y$-direction:

$$(1 - A_2)\Delta\mathbf{u} = \Delta\mathbf{u}^*. \tag{22}$$

The boundary conditions for the intermediate increments are simply $\Delta\mathbf{u}^* = 0$.

Finally a special treatment is required for the cells beyond the free surface, with the aim of preserving the diagonal dominance of the matrices to be inverted.

The matrices must be diagonally dominant with non-zero elements on the principal diagonal. In order to achieve this objective, the velocity points beyond the free surface are considered to have $\Delta\mathbf{u} = 0$; hence the coefficients of the matrices for the equations centred over these points are put equal to zero, one and zero respectively.

The elements of the matrices must be calculated at each time iteration depending on the instantaneous position of the free surface.

### 3.4. *Solution of the Poisson equation*

It is well known that in the fractional step method the continuity equation is rewritten as a Poisson equation. For free surface computations a mixed Neumann–Dirichlet problem must be solved with $\Phi$ and its normal derivatives set equal to zero at the free surface and at the rigid walls respectively.

Usually MAC methods use a point-by-point solver (SOR) mostly because of the difficulties encountered at the free surface. This represents a strong limitation. Indeed on uniform grids the point-by-point solver cannot adequately smooth the low-frequency errors, which results in a large number of iterations for convergence; moreover, on stretched grids this solver often does not converge. Line iterative solvers can alleviate the problem, in particular for stretched grids.

Despite the fact that multigrid techniques represent a class of methods ensuring an excellent rate of convergence, in the MAC methods they have never been employed owing to the difficulties arising at the free surface during the shift from one grid level to the next.

In this paper the Poisson equation is solved using the additive correction multigrid (ACM) technique.[18]

Let us consider the equation:

$$\frac{\partial^2\Phi^{n+1}}{\partial x^2}+\frac{\partial^2\Phi^{n+1}}{\partial y^2}=\frac{1}{\Delta t}\left(\frac{\partial\hat{u}}{\partial x}+\frac{\partial\hat{v}}{\partial y}\right)+\frac{\partial^2\Phi^{n}}{\partial x^2}+\frac{\partial^2\Phi^{n}}{\partial y^2}, \tag{23}$$

with boundary conditions $\partial\Phi^{n+1}/\partial n=0$ at the rigid walls and $\Phi^{n+1}=0$ at the free surface.

According to the notation of Reference 18, equation (23) can be rewritten as

$$a^{\mathrm{P}}_{i,j}\Phi_{i,j}=a^{\mathrm{E}}_{i,j}\Phi_{i+1,j}+a^{\mathrm{W}}_{i,j}\Phi_{i-1,j}+a^{\mathrm{N}}_{i,j}\Phi_{i,j+1}+a^{\mathrm{S}}_{i,j}\Phi_{i,j-1}+\mathrm{RHS}^n, \tag{24}$$

which becomes

$$a^{\mathrm{P}}_{i,j}\Phi_{i,j}-a^{\mathrm{E}*}_{i,j}\Phi_{i+1,j}-a^{\mathrm{W}*}_{i,j}\Phi_{i-1,j}-a^{\mathrm{N}*}_{i,j}\Phi_{i,j+1}-a^{\mathrm{S}*}_{i,j}\Phi_{i,j-1}=\overline{a^{\mathrm{E}}_{i,j}}\Phi_{i+1,j}+a^{\mathrm{W}}_{i,j}\Phi_{i-1,j}$$
$$+\overline{a^{\mathrm{N}}_{i,j}}\Phi_{i,j+1}+\overline{a^{\mathrm{S}}_{i,j}}\Phi_{i,j-1}+\mathrm{RHS}^n, \tag{25}$$

where $a^{\mathrm{E}}_{i,j}=a^{\mathrm{E}^*}_{i,j}+\overline{a^{\mathrm{E}}_{i,j}}$, with $a^{\mathrm{E}^*}_{i,j}=0$ if $\Phi_{i+1}$ is in the $k,l$ block of the coarser grid and $\overline{a^{\mathrm{E}}_{i,j}}=0$ otherwise. The ACM technique envisages the sum of equation (25) over the blocks of the coarser grid and the solution of the resulting equations for a correction $\delta$.

If one sums equation (25) over the $k,l$ block of the coarser grid, the result will be

$$\sum_M D_{i,j}\Phi_{i,j}=\sum_M\left(\overline{a^{\mathrm{E}}_{i,j}}\Phi_{i+1,j}+\overline{a^{\mathrm{W}}_{i,j}}\Phi_{i-1,j}+\overline{a^{\mathrm{N}}_{i,j}}\Phi_{i,j+1}+\overline{a^{\mathrm{S}}_{i,j}}\Phi_{i,j-1}+\mathrm{RHS}^n\right), \tag{26}$$

where $M$ is the number of cells of the fine grid within the $k,l$ block of the coarser grid and $D_{i,j}=a^{\mathrm{P}}_{i,j}-a^{\mathrm{E}^*}_{i,j}-a^{\mathrm{W}^*}_{i,j}-a^{\mathrm{N}^*}_{i,j}-a^{\mathrm{S}^*}_{i,j}$.

If $\tilde{\Phi}_{i,j}$ is the updated value of the computational pressure during the iterative cycle, after the level shift one can write $\Phi_{i,j}=\tilde{\Phi}_{i,j}+\delta_{k,l}$. If one replaces $\Phi_{i,j}$ with $\tilde{\Phi}_{i,j}+\delta_{k,l}$ in equation (26), after some manipulations the result will be

$$\bar{a}^{\mathrm{P}}_{k,l}\delta_{k,l}=\bar{a}^{\mathrm{E}}_{k,l}\delta_{k+1},+\bar{a}^{\mathrm{W}}_{k,l}\delta_{k-1,l}+\bar{a}^{\mathrm{N}}_{k,l}\delta_{k,l+1}+\bar{a}^{\mathrm{S}}_{k,l}\delta_{k,l-1}+B_{k,l}, \tag{27}$$

where

$$\bar{a}^{\mathrm{P}}_{k'l}=\sum_M D_{i,j},\quad \bar{a}^{\mathrm{E}}_{k,l}=\sum_M\overline{a^{\mathrm{E}}_{i,j}},\quad \ldots,\quad B_{k,l}=\sum_M(\nabla^2\tilde{\Phi}-\mathrm{RHS}^n)_{i,j}. \tag{28}$$

The implementation of ACM is rather straightforward and does not require any manipulation of the boundary conditions, the latter being included implicitly in the coefficients of the fine grid equations.

In the present work the computational domain contains $2^{P1} \times 2^{P2}$ control volumes ($P1$ and $P2$ are integer numbers) and the selection of the number of levels is made so as to ensure that the coarsest grid contains two blocks at least in one direction. Afterwards a V-cycle is performed and two or three SOR cycles are used at each grid level.

It was observed that, compared with an SOR procedure, the ACM technique applied to a free surface computation reduces the solution time by a factor of seven to nine on a 64 × 64 stretched grid.

### 3.5. *Free surface*

The domain of integration of the governing equations is divided into two parts by markers which identify the instantaneous position of the free surface.

The markers are located at each half-cell as shown in Figure 2 and advance in time by means of equation (4). This treatment results in an improvement in volume conservation, because interpolations are no longer required for the flagging of the velocities and pressure points.

The velocities of the markers are calculated by bilinear interpolation between the neighbouring values. An extrapolation of the velocities beyond the free surface must therefore be performed in advance. This operation is done according to TUMMAC-V.[8]

As shown in Figure 3, six cases are considered for the extrapolation of one velocity component. Figure 3 refers to the $v$-component, but the procedure is the same for the $u$-component as well.

The extrapolation is repeated twice owing to the large number of points involved in the HLPA scheme.

The solution of the pressure equation is performed as previously described. For free surface cells the condition $\Phi \approx P = 0$ at the free surface is enforced through the calculation of the distance $\tau$ (see Figure 4) between the pressure point where the equation has to be discretized and the free surface itself. As an example, with reference to Figure 4 the Poisson equation centred at $i$, $j$ will be

$$\frac{1}{\Delta x}\left(\frac{0-\Phi_{i,j}}{\tau_2}-\frac{\Phi_{i,j}-0}{\tau_1}\right)+\frac{1}{\Delta y}\left(\frac{0-\Phi_{i,j}}{\tau_3}-\frac{\Phi_{i,j}-\Phi_{i,j-1}}{\Delta y}\right)=\text{RHS}. \tag{29}$$

Finally, equation (4) is applied to advance the markers and is solved by means of a forward in time and upwind in space finite difference algorithm.

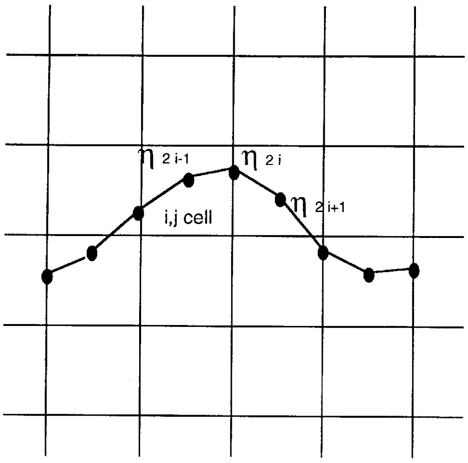

Figure 2. Position of markers on instantaneous free surface profile

**Case 1** : $v_{i,j} = 0.5\,(v_{i-1,j} + v_{i+1,j})$ **Case 2** : $v_{i,j} = (\Delta y\, v_{i-1,j} + \Delta x\, v_{i,j-1}) / (\Delta x + \Delta y)$

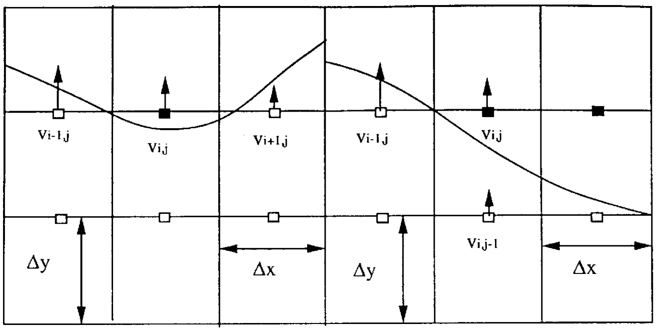

**Case 3** : $v_{i,j} = (\Delta y\, v_{i+1,j} + \Delta x\, v_{i,j-1}) / (\Delta x + \Delta y)$ **Case 4** : $v_{i,j} = v_{i,j-1}$

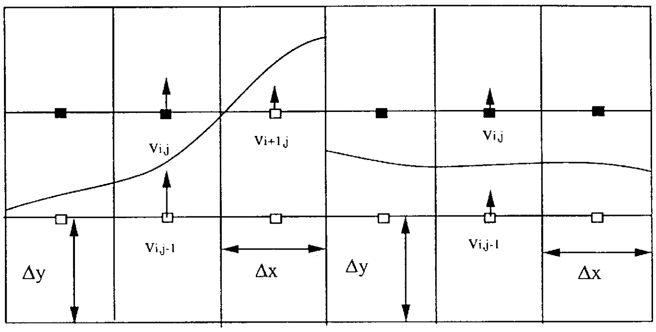

**Case 5** : $v_{i,j} = v_{i-1,j}$ **Case 6** : $v_{i,j} = v_{i+1,j}$

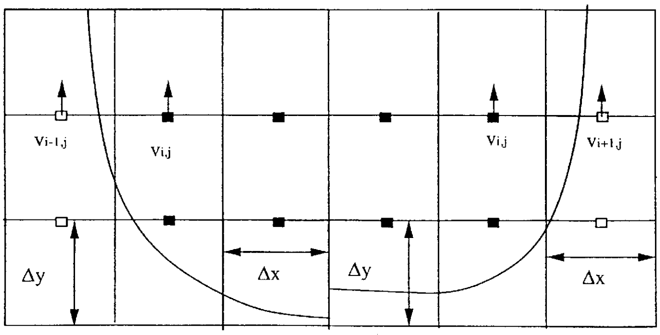

Figure 3. Extrapolation of *v*-component of velocities outside liquid portion in computational domain: black box, velocity points outside liquid portion; white box, velocity points within liquid portion. For the sake of simplicity the figure refers to a uniform grid, though the generalization to stretched grids is straightforward

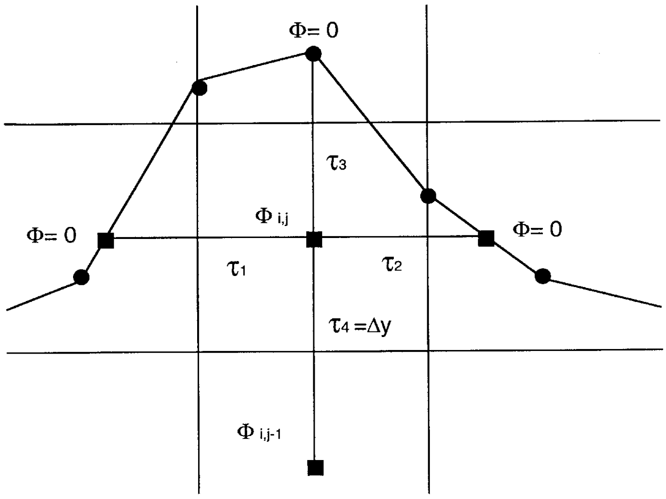

Figure 4. ‘Irregular stars’ ($\tau$) used for discretization of Poisson equation at free surface

With reference to Figure 2 it follows that

$$\eta_{2i}^{n+1} = \eta_{2i}^{n} + v_{(\mathrm{m})2i}\Delta t - \Delta t \max(u_{(\mathrm{m})2i}, 0)\frac{\eta_{2i}^{n} - \eta_{2i-1}^{n}}{0{\cdot}5\Delta x_i} - \Delta t \max(-u_{(m)2i}, 0)\frac{\eta_{2i+1}^{n} - \eta_{2i}^{n}}{0{\cdot}5\Delta x_{i+1}},$$

$$\eta_{2i-1}^{n+1} = \eta_{2i-1}^{n} + v_{(\mathrm{m})2i-1}\Delta t - \Delta t \max(u_{(m)2i-1}, 0)\frac{\eta_{2i-1}^{n} - \eta_{2i-2}^{n}}{0{\cdot}5\Delta x_i} - \Delta t \max(-u_{(m)2i-1}, 0)\frac{\eta_{2i}^{n} - \eta_{2i-1}^{n}}{0{\cdot}5\Delta x_i}, \tag{30}$$

being $u_{(\mathrm{m})}$ and $v_{(\mathrm{m})}$ the $x$- and $y$-components of the velocity of the markers respectively.

## 4. NUMERICAL RESULTS

This section is divided into two main subsections. In the first one numerical tests on the algorithm are discussed. The second subsection thoroughly analyses a case of practical interest in engineering.

### 4.1. Numerical Tests

First numerical tests were performed in order to evaluate the consistency of the algorithm. In particular, grid sensitivity tests were carried out for several values of the kinematic viscosity and for different kinds of external excitation. The effect of the time increment $\Delta t$ on the accuracy of the solution was then analysed for a given grid size and Reynolds number.

The following case was considered first: a rectangular (1 m breadth, 0·5 m height) tank is suddenly accelerated along the horizontal direction and the liquid motion is recorded till a steady state condition is reached. The steady state condition corresponds to a flat free surface profile inclined at an angle equal to $\tan^{-1}(A_x/g)$, where $A_x$ is the horizontal acceleration, which is kept constant during the computation, and $g$ is the gravitational acceleration. In this test $A_x$ is equal to 1 m s$^{-2}$ and the components of the body forces are $B_x = -A_x$ and $B_y = -g$ in equations (2) and (3) respectively. The Reynolds number ($Re = (b^3 g)^{1/2}/\nu$, with $b$ denoting the tank breadth) is chosen equal to 313. The liquid depth is chosen equal to 0·21 m and three different uniform grids (16 × 16, 32 × 32, 64 × 64) are used. The maximum allowed time step is chosen equal to 0·005 s and the Courant number equal to 0·5. The wave height at the left side wall and the percentage of volume variation during the computation versus time are plotted in Figure 5 and 6 respectively. It can be observed (Figure 5) that

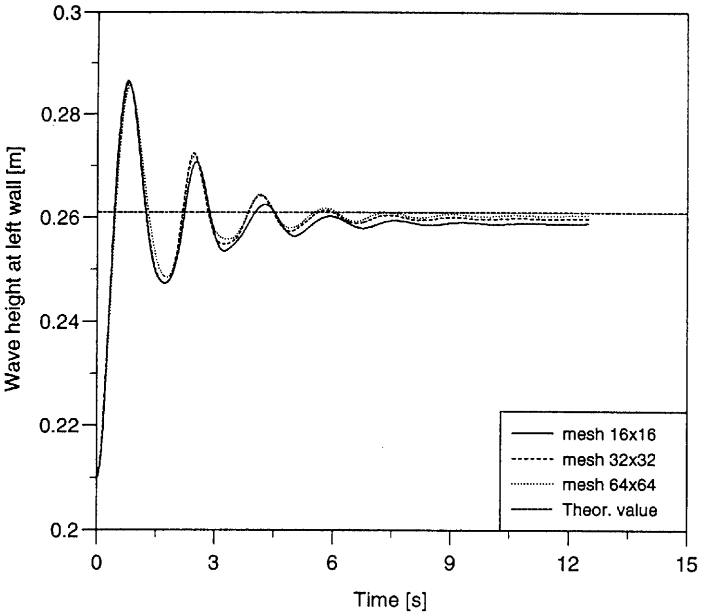

Figure 5. Wave height at left side wall versus time using three different uniform meshes (constant horizontal acceleration $A_x = 1\ \mathrm{m\ s^{-2}}$, $\nu = 0{\cdot}01\ \mathrm{m^2\ s^{-1}}$)

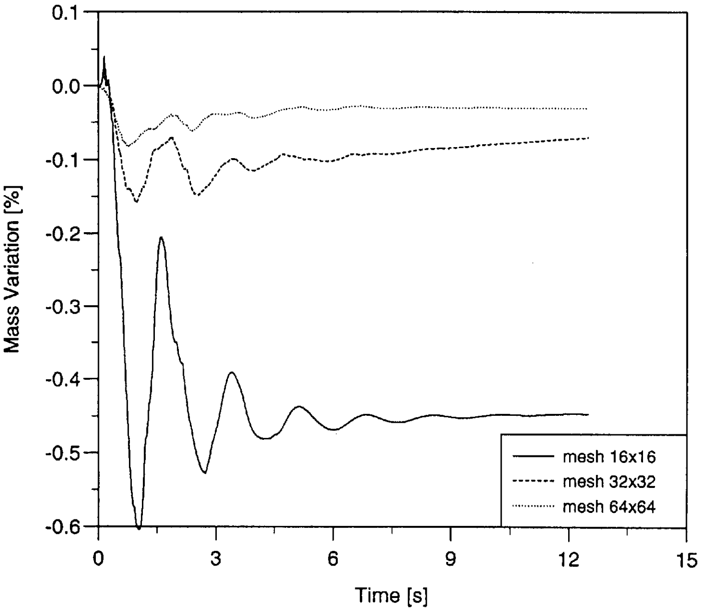

Figure 6. Percentage of mass variation versus time for simulations of Figure 5

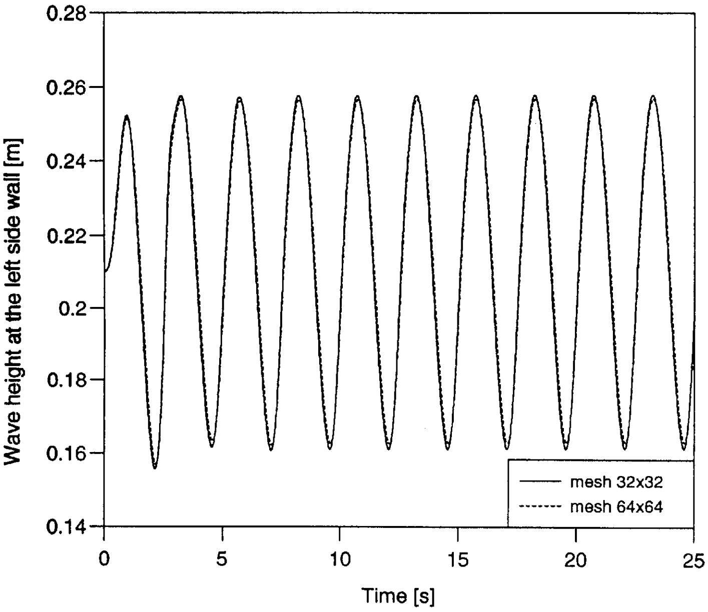

Figure 7. Wave height at left side wall versus time using two different uniform meshes (sinusoidal sway motion, sway amplitude 0·1 m, sway period 2·5 s, $\nu = 0{\cdot}01$ s$^2$ s$^{-1}$

upon increasing the number of grid points, the difference between the analytical and the numerical solution is less than 0·27% in the case of the 64 × 64 grid.

Moreover, the analysis of the transient wave motion indicates that the reduction of the grid spacing leads to a more accurate prediction of the wave speed. As regards the computation on the 64 × 64 grid, a travelling wave moving with a period close to the theoretical value—the difference being less than 0·4%—is observed. If one looks at Figure 6, the increase in the number of points results in a reduction of the volume variation during the computation.

The previous tank was then forced into a sinusoidal large-amplitude (sway amplitude = 0·1 m) off-resonance (sway period 2·5 s) horizontal motion using the same Reynolds number as in the previous computations and uniform 32 × 32 and 64 × 64 grids. In this case the components of the body forces will be $B_x = -0{\cdot}1(2\pi/2{\cdot}5)^2 \sin[(2\pi/2{\cdot}5)t]$ and $B_y = -g$.

Figure 7 shows that a periodic motion condition is reached and that, using two grids, there are no appreciable differences in the wave height at the left side wall. The vertical component of the velocity at the $y = 0{\cdot}156$ m location at $t = 25$ s is plotted in Figure 8 for the 32 × 32 and 64 × 64 grids. The results are satisfactory in this case as well.

Then, in order to evaluate the effect of stretching on the accuracy of the solution, computations were carried out for the 32 × 32 and 64 × 64 stretched grids using $Re = 939{\cdot}4$ ($\nu = 0{\cdot}0033$ m$^2$ s$^{-1}$). The stretching was computed as follows:

$$x(i) = b\left(\frac{\tanh\left[a_x\left(i - j_x/2\right)\right]}{\tanh\left[\left(a_x j_x/2\right)\right] - \tanh\left[\left(-a_x j_x/2\right)\right]}\right), \tag{31}$$

$$y(i) = l_y\left(1 + \frac{\tanh[a_y(i - j_y)]}{\tanh[(a_y j_y)]}\right), \tag{32}$$

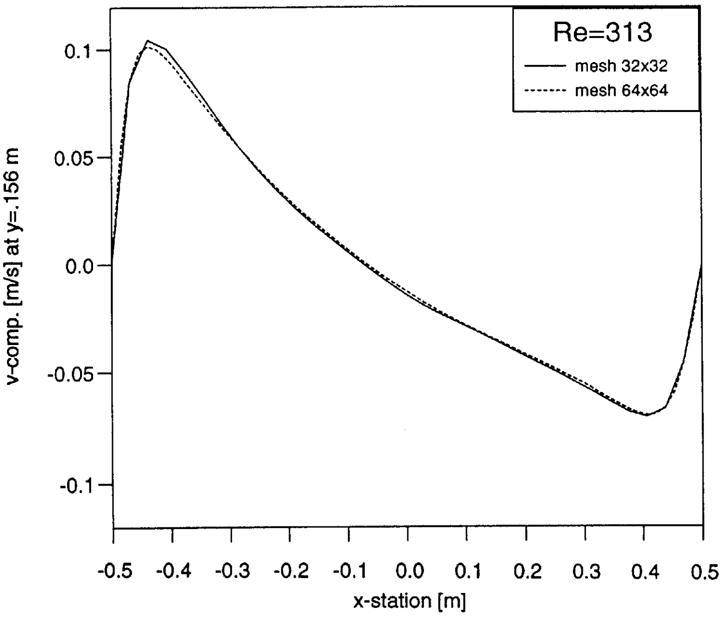

Figure 8. $v$-Component of velocity at $y=0{\cdot}156$ m location at $t=25$ s for simulations of Figure 7

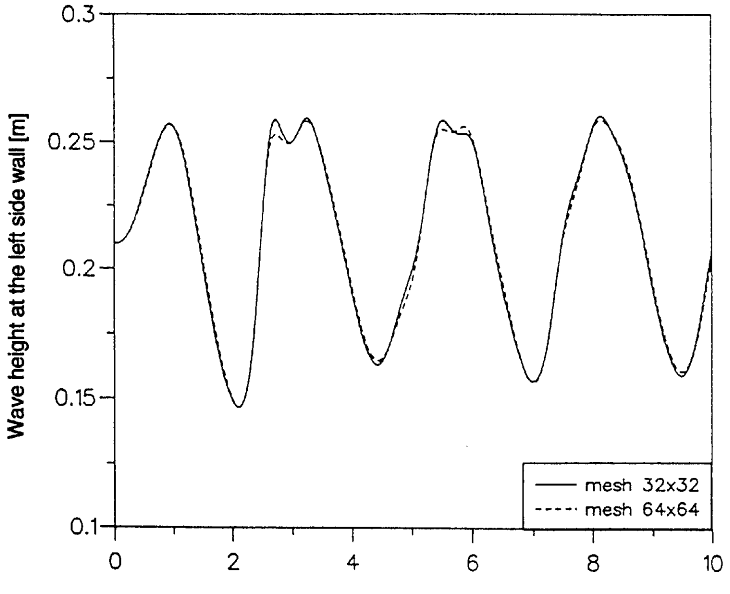

Figure 9. Wave height at left side wall versus time using two different stretched grids (sinusoidal sway motion, sway amplitude 0·1 m, sway period 2·5 s, $\nu=0{\cdot}0033$ m$^2$ s$^{-1}$)

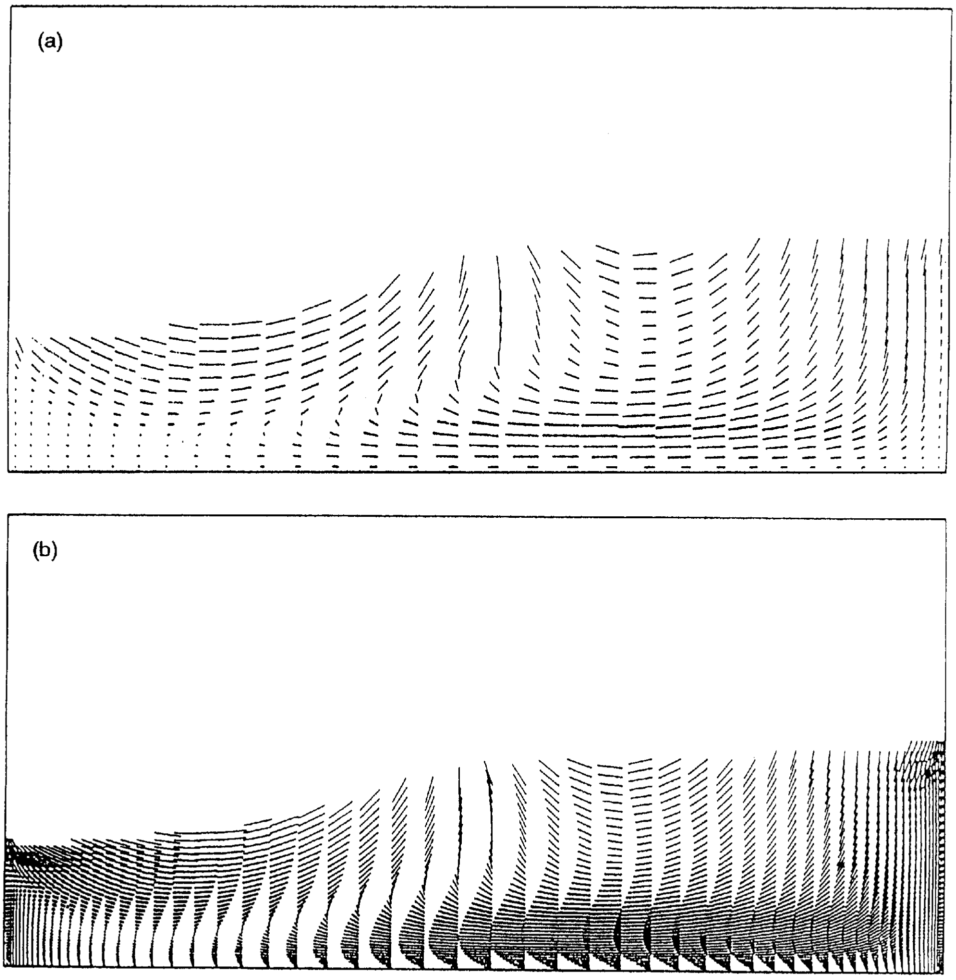

Figure 10. Computed velocity field at $t = 2{\cdot}5$ s (sinusoidal sway motion, sway amplitude 0·1 m, sway period 2·5 s, $\nu = 0{\cdot}0033\ \mathrm{m^2\ s^{-1}}$): (a) 32 × 32 stretched grid; (b) 64 × 64 stretched grid

where $l_y$ is the height of the tank, $j_x$ and $j_y$ are the numbers of cells in the $x$- and $y$-direction respectively and $a_x$ and $a_y$ are coefficients which distribute the dimensions of the cells inside the domain.

An increase in $a_x$ and $a_y$ reduces the grid size near the walls of the tank. In the cases that are being considered, a compromise has to be reached between the location of a large number of points near the walls, necessary for a good evaluation of the boundary layer characteristics, and the grid fineness in the middle of the tank, necessary to avoid an excessive smoothing of the free surface waves, which may occur when large stretching is employed.

Figure 9 shows the wave height at the left side wall for the two above-mentioned grids. The results are once again satisfactory. Finally the velocity vector fields computed at $t = 2{\cdot}5$ s on both the 32 × 32 and 64 × 64 grids are shown in Figure 10.

As already mentioned, a second-order discretization in both time and space was employed for the solution of the governing equations, nevertheless the present treatment of the free surface can reduce the order of accuracy of the algorithm. Thus, in order to evaluate the effect of the time step on the accuracy of the solution, several computations were carried out using a 64 × 64 stretched grid, $Re = 1565{\cdot}7$ ($\nu = 0{\cdot}002$ m$^2$ s$^{-1}$) and the following values of the time increment: $\Delta t = 0{\cdot}001, 0{\cdot}002, 0{\cdot}004$ and 0·008 s. The same tank and periodic sway excitation as in the previous test were used.

Figures 11(a)–11(e) show the time evolution of the wave height at two locations ($x = -0{\cdot}5$ and $-0{\cdot}25$ m), the components of the velocity field at $x = 0, y = 0{\cdot}0398$ and the pressure computed at $x = 0, y = 0{\cdot}0398$ m.

The distribution of the vertical component of velocity in the $y = 0{\cdot}0398$ m section at $t = 6$ s is plotted in Figure 12. Appreciable differences appear for $\Delta t = 0{\cdot}008$ s. In particular, in this case a weak smoothing of the velocities (Figure 12) and of the pressure (Figure 11(e)) is observed. If one looks at the time evolution of the liquid height at the left wall (Figure 11(a)), a numerical noise appears for $\Delta t = 0{\cdot}008$ s even if the characteristics of the transient wave motion, i.e. the overlapping of short travelling waves on the standing wave, are well predicted. The analysis of the results showed that the algorithm is first-order-accurate in time.

As previously outlined, the main feature of the improved MAC method proposed herein is the accurate evaluation of the viscous stress at the solid boundaries in free surface computations. As an example, a computation in a case of high-filling conditions (liquid depth/tank breadth ratio $\eta/b = 0{\cdot}3$) for a large-amplitude free surface motion shows very interesting boundary layer patterns. In this case the tank is subjected to roll motion through the origin of the frame of reference, so that the body forces read (see also Figure 1):

$$B_x = -g\sin[\Theta(t)] + \ddot{\Theta}(t)r_y + \dot{\Theta}(t)^2 r_x + 2v\dot{\Theta}(t), \tag{33}$$

$$B_x = -g\cos[\Theta(t)] + \ddot{\Theta}(t)r_x + \dot{\Theta}(t)^2 r_y - 2u\dot{\Theta}(t), \tag{34}$$

where $r_x$ and $r_y$ are the components of the vector $\mathbf{r}$ along the $x$- and $y$-axis respectively and $\dot{\Theta}(t)$, $\Theta(t)$ and $\ddot{\Theta}(t)$ are the roll angle, velocity and acceleration respectively.

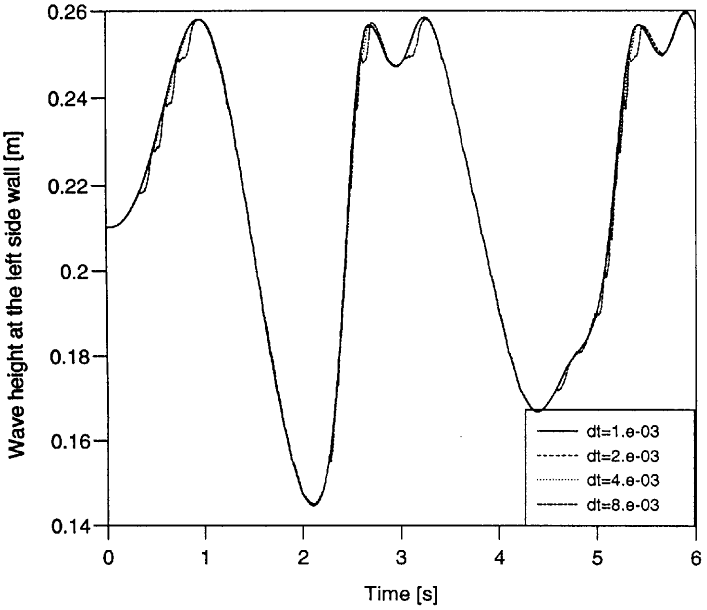

Figure 11(a). Time domain evolution of wave height at left side wall using four different time steps (64 × 64 stretched grid, $\nu = 0{\cdot}002$ m$^2$ s,$^{-1}$ sway amplitude 0·1 m, sway period 2·5 s)

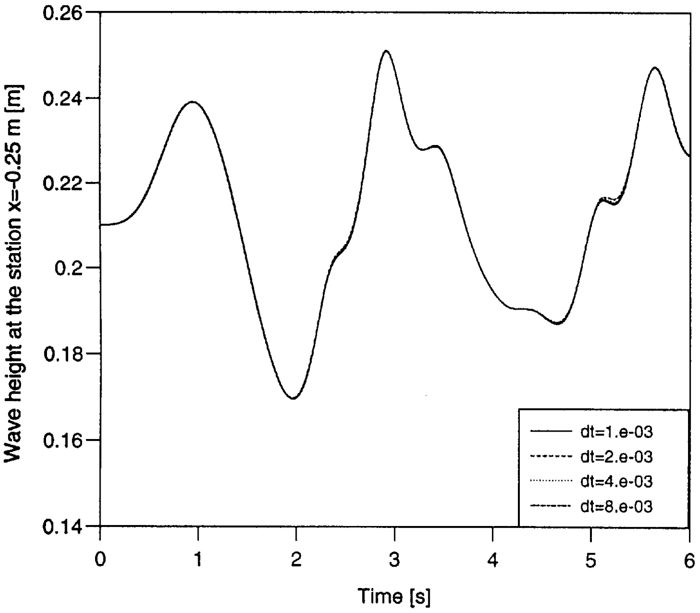

Figure 11(b). Time domain evolution of wave height at $x=0{\cdot}25$ m location using four different time steps ($64 \times 64$ stretched grid, $\nu=0{\cdot}002$ m$^2$ s,$^{-1}$ sway amplitude 0·1 m, sway period 2·5 s)

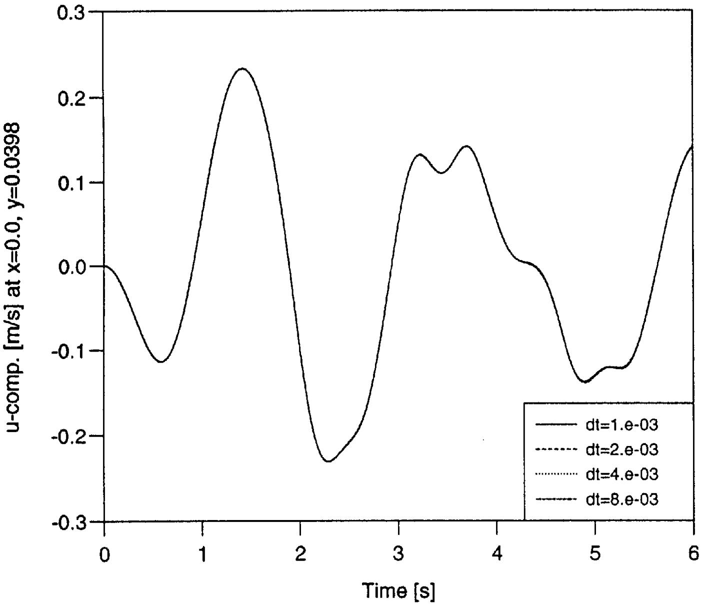

Figure 11(c). Time domain evolution of $u$-component of velocity at $x=0$, $y=0{\cdot}0398$ m using four different time steps ($64 \times 64$ stretched grid, $\nu=0{\cdot}002$ m$^2$ s,$^{-1}$ sway amplitude 0·1 m, sway period 2·5 s)

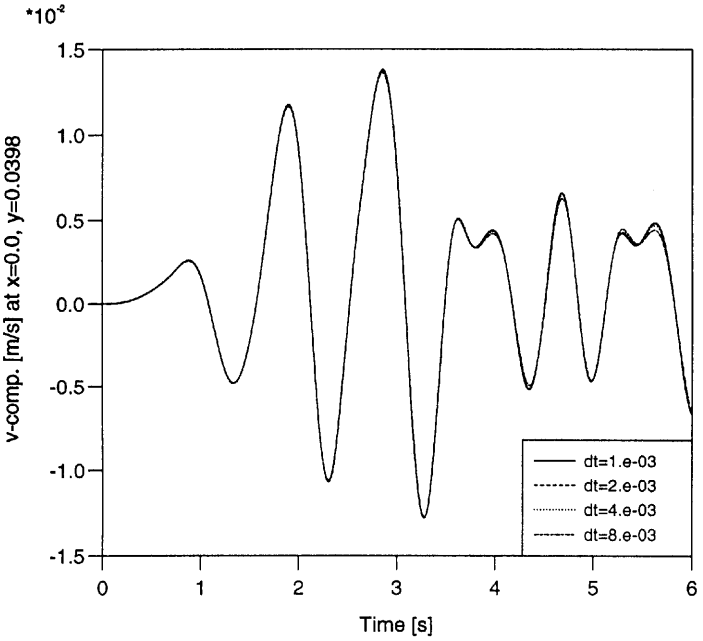

Figure 11(d). Time domain evolution of $v$-component of velocity at $x = 0$, $y = 0{\cdot}0398$ m wall using four different time steps ($64 \times 64$ stretched grid, $\nu = 0{\cdot}002$ m$^2$ s,$^{-1}$ sway amplitude 0·1 m, sway period 2·5 s)

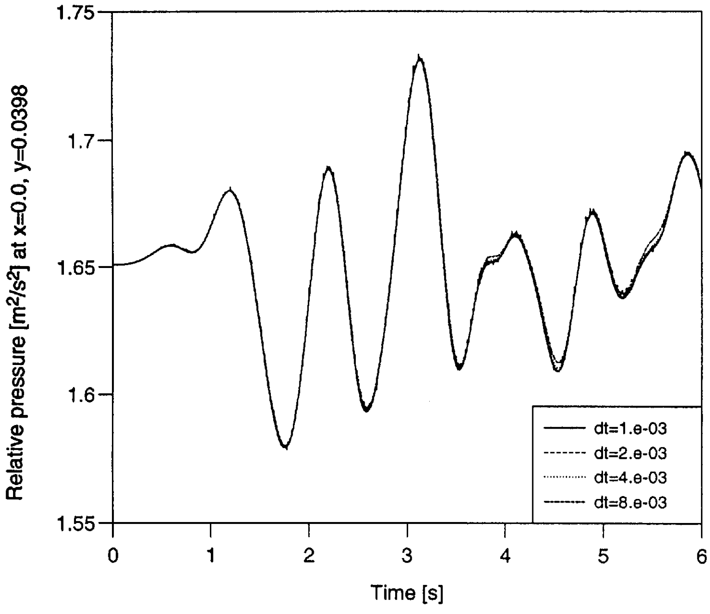

Figure 11(e). Time domain evolution of relative pressure at $x = 0$, $y = 0{\cdot}0398$ m using four different time steps ($64 \times 64$ stretched grid, $\nu = 0{\cdot}002$ m$^2$ s,$^{-1}$ sway amplitude 0·1 m, sway period 2·5 s)

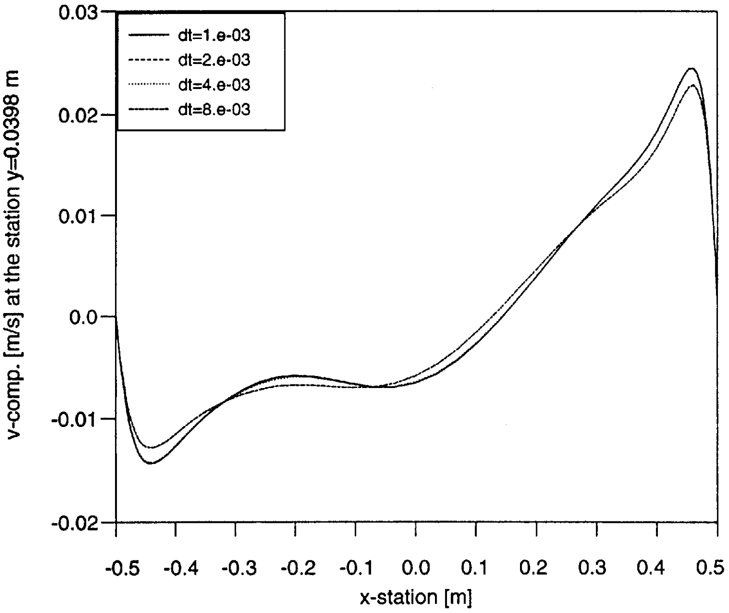

Figure 12. $v$-component of velocity at $y$=0·0398 m location at $t = 6$ s using four different time steps (grid, viscosity and characteristics of sinusoidal sway motin are same as in Figure 11)

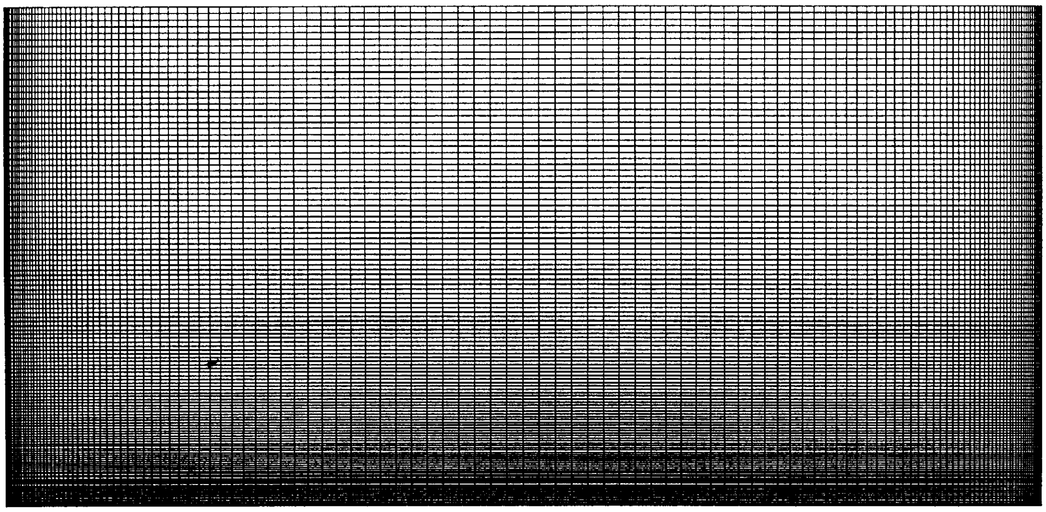

Figure 13. 128 × 128 stretched grid employed for evaluation of boundary layer characteristics using two different values of kinematic viscosity

The motion is sinusoidal with maximum amplitude equal to 2° and period equal to 1·76 s, so that $\Theta(t) = (2\pi/180)\sin[(2\pi/1{\cdot}76)t]$. The computations were carried out on a 128 × 128 stretched grid (Figure 13), with two different liquids as in Table I.

Owing to the small values of viscosity employed, the computations were stopped at $t = 5.28$ s, which corresponds to three periods of excitation, in order to reach a fully developed laminar flow condition. Figure 14a shows the $u$-component of velocity recorded at the $x = 0$ location near the

Table I. Liquids used in computations and their kinematic viscosities

| Liquid | Kinematic viscosity ($10^{+6}$ m$^2$ s$^{-1}$) |
|---|---|
| Glycerol/water 63% | 11·5 |
| Water | 1·0 |

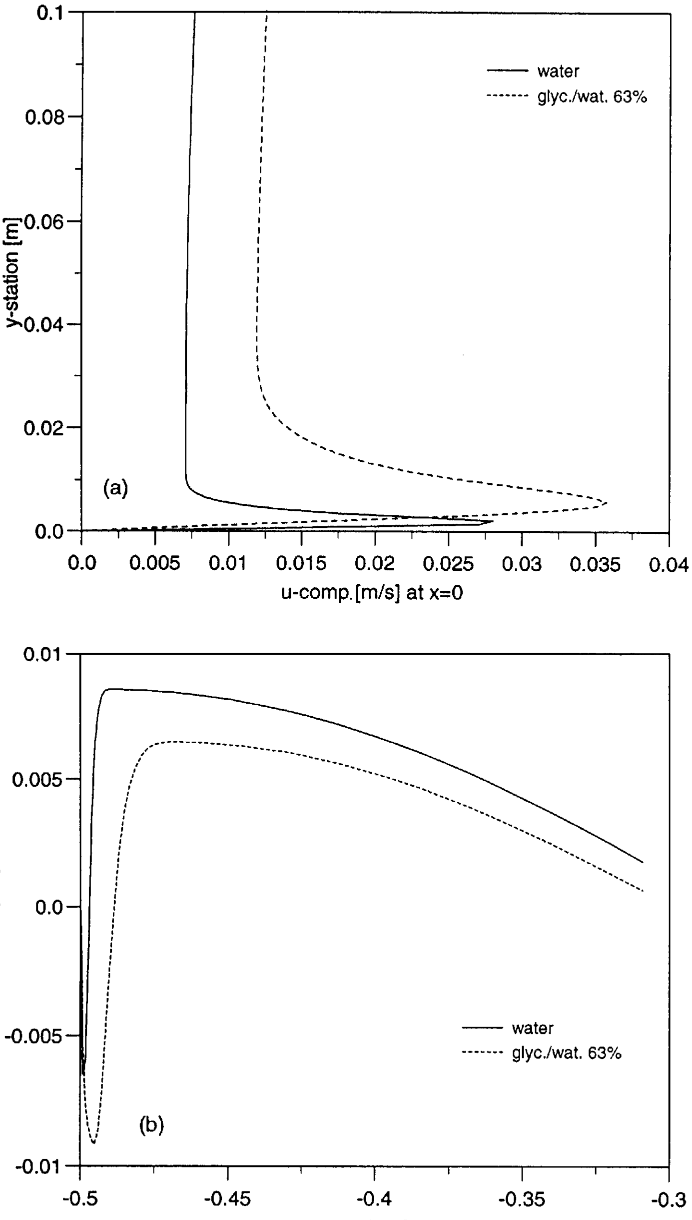

Figure 14. Distribution at $t = 5{\cdot}28$ s of (a) $u$-component of velocity at location $x = 0$ near bottom of tank and (b) $v$-component of velocity at location $y = 0{\cdot}1$ m nearby left side wall of tank ($\eta/b = 0{\cdot}3$, sinusoidal roll motion around $x = 0$, $y = 0$, roll period 1·76 s, roll amplitude 2°)

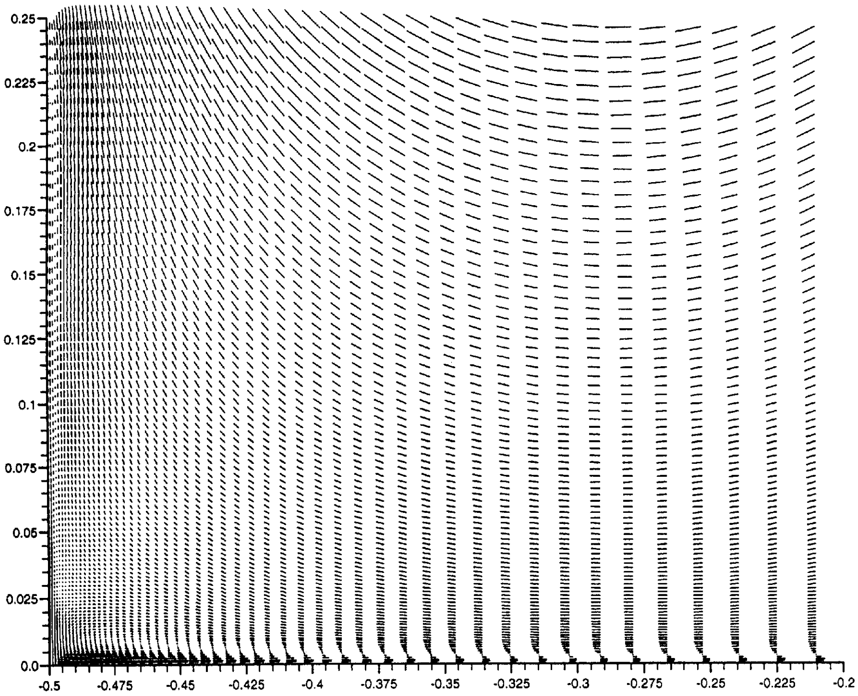

Figure 15. Sketch of velocity field showing streaming layer phenomenon for simulation of Figure 14 (low viscosity case, $\nu = 1 \times 10^{-6}$ m$^2$ s$^{-1}$)

bottom of the tank. It can be noticed that the velocity profile is rather different from that which could be obtained in the case of steady state calculations. The thickness of the boundary layer decreases significantly with increasing Reynolds number. The $v$-component of velocity recorded 0·10 m above the bottom near the left side wall (Figure 14(b)) shows a typical feature of streaming layer phenomena[19] which results in the inversion of the velocity profile within the boundary layer. The phenomenon is clearly shown in Figure 15.

### *4.2. Numerical and experimental analysis of water sloshing in a rectangular tank in roll motion*

Liquid sloshing in containers has represented an important problem in transportation engineering since the 1960s. The sloshing induced overturning moment can affect ship stability when large amounts of liquid cargoes are shipped on board. On the other hand the induced dynamic impulsive pressures often cause structural damage in the bulkheads of the tanks. The numerical simulation of such a phenomenon requires an algorithm that can simulate highly distorted free surface waves, including the splashes against the vertical walls of the flooded tank. As widely shown in the past, MAC-type methods are effective in simulating such a complex phenomenon. Unfortunately, since they cannot accurately solve the viscous stress at the solid boundaries, practical computations often refer to the solution of the Euler equations[20] (free slip condition at the solid boundaries), sometimes leaving the role of stabilizing the numerical solution[21] to the diffusive terms. These procedures turns out to be inaccurate, especially when the tanks are equipped with internal baffles so that the velocity field is strongly affected by viscosity. The need for an accurate simulation of liquid sloshing has been outlined in recent works. In particular it has been clearly maintained[12] that improvements are needed to accelerate the computations so that a turbulence model for an accurate simulation of high Reynolds flows can also be included.

As previously stated, the underlying idea of the improved MAC method proposed in this paper is to overcome the above-mentioned limitations while maintaining the advantages offered by the MAC methods in treating distorted free surface patterns.

In the second stage of the work the physical analysis of water sloshing in rectangular containers was carried out. A turbulence model was included in the algorithm in order to simulate high-Reynolds flows.

The choice of a suitable turbulence model is a difficult task. The physical problem is unsteady, the mean velocity is zero and there is no dominant flow direction. For these reasons the algebraic Baldwin–Lomax model, widely applied in ship hydrodynamics, cannot be used. On the other hand, in the opinion of the author, the implementation of a $k-\varepsilon$ model is too difficult for several reasons. First, it is not clear how the kinetic turbulent energy and the dissipation $\varepsilon$ at the liquid–solid interface and at the free surface should be treated. Moreover the implementation of such a model presupposes the knowledge of too many empirical constants which have to be adjusted to the physical problem under consideration.

For these reasons it was decided to apply an algebraic SGS turbulence model as modified by Miyata *et al.*[9] into a two dimensional form. Obviously these considerations are not exhaustive and a lot of effort should be devoted to the search for an accurate turbulence model for such simulations. Nevertheless, to the knowledge of the author, no attempts have been made so far to simulate large amplitude water sloshing with an algorithm that includes a turbulence model.

The study was performed for three filling conditions, including both the shallow water and the high depth cases in the whole range of frequencies of practical interest. In the high depth case a baffled configuration was also analysed.

In order to validate the numerical results, experimental tests were carried out at the Hydrodynamic Laboratories of the Department of Hydraulics of the University of Rome.

A rectangular 0·50 × 0·5 × 0·25 $m^3$ tank made of Plexiglass was used (Figure 16). The tank was placed on a massive support anchored to the floor and connected to an AC motor (140 W) by means

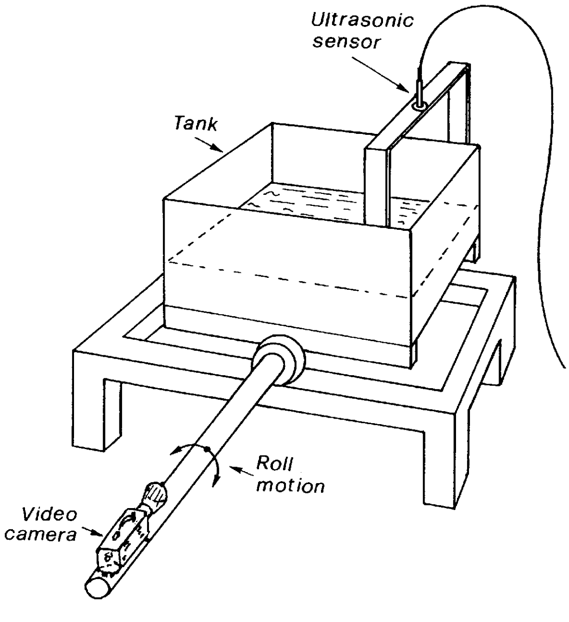

Figure 16. Schematic representation of experimental set-up

of a four-bar linkage. The motor transmits roll motion by means of an axis located 0·048 m below the bottom of the tank. The maximum allowable frequency of the motor is 6·78 rad/s$^{-1}$.

The tank motion is two dimensional and, with the exception of some special cases, the liquid motion inside the tank was observed to be two-dimensional as well.

A wave height recorder composed of an ultrasonic sensor (Honeywell S9432-AUDS) placed 0·70 m above the bottom of the tank and 0.10 m from the right side wall was used.

Finally the wave patterns were recorded by means of a digital video-recorder located 1·5 m away from the tank. The records were then digitized in order to derive the free surface profiles for the cases of interest.

The filling ratios investigated ($\eta/b = 0{\cdot}005, 0{\cdot}15, 0{\cdot}2$) are indicative of three different situations: a first one in which resonant hydraulic jumps are recorded; a second one with large travelling waves impacting against the vertical walls; and a third one characterized by the presence of large-amplitude standing waves.

First free oscillation tests were carried out numerically. Such computations are indicative of the ability of the algorithm to predict the wave speed correctly. As initial conditions the fluid is at rest, the pressure distribution hydrostatic and the free surface profile inclined at an angle of 5°. In these tests the filling ratio $\eta/b = 0{\cdot}1$ was also investigated. The time evolution of the liquid height at the left side wall was recorded and afterwards the natural period of oscillation was calculated as the difference between the time instants at which the liquid height at the left side wall reaches the maximum value. These periods were measured for several cycles of oscillation and the mean value was calculated. Figure 17 shows the computed natural period versus $\eta/b$ together with the values derived from the linear theory. It can be observed that the numerical results well agree with the analytical ones in the whole range of liquid depths investigated. According to physical observations,[22,23] the analysis of the decay curves shows that for $\eta/b$ up to 0·1 the liquid motion is strongly damped after the first oscillation, basically because of the generation of a hydraulic jump

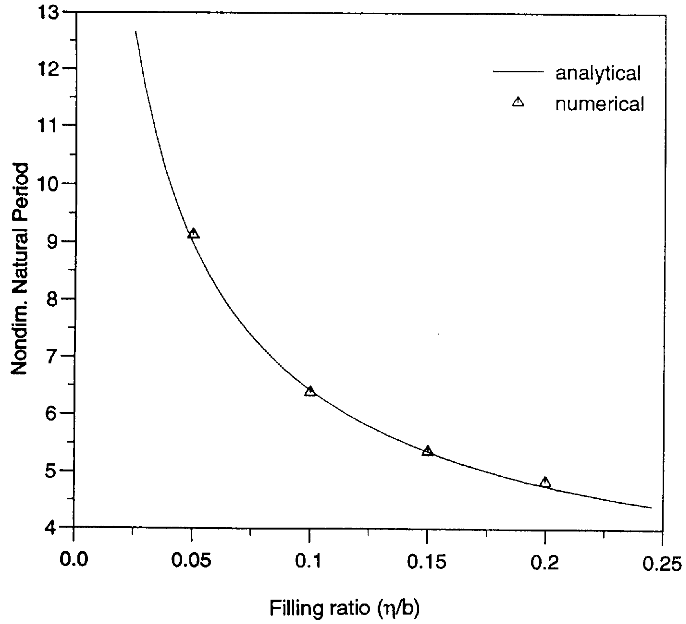

Figure 17. Analytical (linear potential theory) and computed non-dimensional natural period versus filling ratio ($\eta/b$) inside tank

which impacts against the tank walls thereby dissipating energy. On the other hand the increase in the liquid depth inside the tank makes the wave mode shift from a hydraulic jump to a travelling wave ($\eta/b = 0{\cdot}15$) until it reaches a standing wave in the case of $\eta/b = 0{\cdot}2$. In the last two cases the free surface motion turns out to be less damped than in the case of shallow water.

Later on numerical computations were performed with the tank located at $d = 0{\cdot}048$ m above the centre of oscillation as in the experiments. Thus the body forces will be

$$B_x = -g\sin[\Theta(t)] + \ddot{\Theta}(t)(r_y + d) + \dot{\Theta}(t)^2 r_x + 2v\dot{\Theta}(t), \tag{35}$$

$$B_y = -g\cos[\Theta(t)] + \ddot{\Theta}(t)(r_x) + \dot{\Theta}(t)_2(r_y + d) - 2u\dot{\Theta}(t). \tag{36}$$

Two maximum roll amplitudes were investigated, 0·9° and 1·7°. The choice of small amplitude roll motion was made in order to avoid water outflow from the tank during the experiments. Nevertheless, owing to the fact that the tank bottom is located above the rolling centre, large travelling waves or hydraulic jumps were observed in both the computations and the experiments. In order to compare numerical and experimental results, the same law of motion as in the experiments was included in the computer code. However the experimental device provides a sinusoidal roll motion, velocity and acceleration for roll amplitudes within 3°.

As regards the case $\eta/b = 0{\cdot}05$, the numerical and experimental non-dimensional wave heights $(\eta_{\max} - \eta_{\min})/b$ versus the roll frequency (hereafter referred to as $\Omega$) are plotted in Figure 18. It has to be pointed out that a steady state oscillation is rarely obtained. Hence the non-dimensional wave heights presented hereafter are always considered to be mean values over an adequately long time interval.

Numerical results and experimental data show that even if the first natural frequency predicted by the linear theory is equal to 3·1 rad $s^{-1}$ the resonance zone enlarges with increasing roll amplitude. The behaviour of the numerical solution at $\Omega = 3{\cdot}98$ rad $s^{-1}$ for a roll amplitude equal to 0·9°

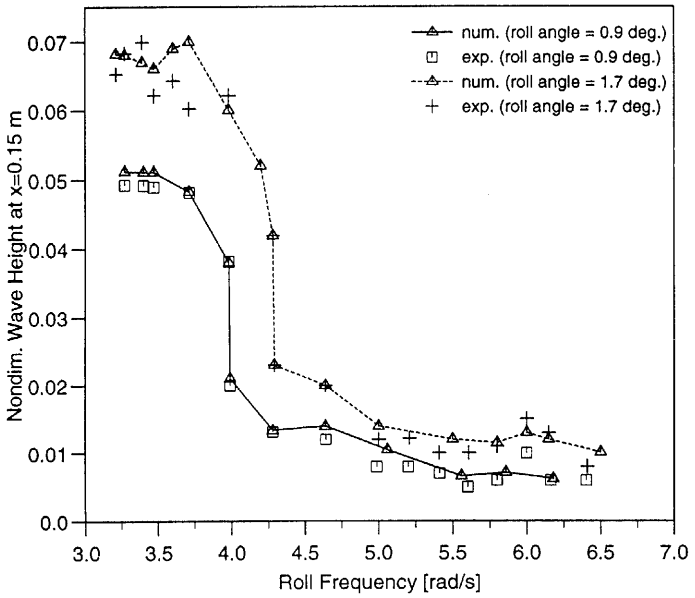

Figure 18. Numerical and experimental non-dimensional wave height at locatin $x = 0{\cdot}15$ m versus roll frequency for two roll amplitudes ($\eta/b = 0{\cdot}05$)

confirms the experimental results which show the non-linear features of the physical system.[24] In particular, at $\Omega = 3{\cdot}98$ rad s$^{-1}$ two stable wave modes can be excited (Figure 19), a hydraulic jump and a standing wave, and it is possible to shift from the first mode to the second one by introducing a small perturbation in the system. In both the experiment and the computation the perturbation was introduced by continuously varying the roll frequency from 4 to 3·98 rad s$^{-1}$ after a steady state oscillation was reached. As in the previous case the same phenomenon was observed at $\Omega = 4{\cdot}28$ rad s$^{-1}$ for the roll amplitude equal to 1·7°.

The tests were also carried out in the range of high frequencies in order to analyse the liquid motion in the zone of the second resonant frequency ($\Omega = 6{\cdot}12$ rad s$^{-1}$). At this value only a smooth resonance peak appears.

The numerical and experimental resonant wave patterns at four time instants are presented in Figure 20, which clearly shows the agreement between the free surface profiles predicted by the computations and those observed in the experiments.

As previously highlighted, the main effect of an increase in the liquid depth inside the tank ($\eta/b = 0{\cdot}15$) lies in the variation of the resonant wave mode from a hydraulic jump to a large travelling wave (Figure 21). The resonance zone is narrower compared with the previous case and jumps of wave amplitudes in the frequency domain are no longer observed (Figure 22). For this filling ratio the analysis for a roll amplitude equal to 1·7° was restricted to an off-resonance low frequency zone, mainly owing to large water outflow in the case of resonant motion.

Finally, the filling ratio 0·2 was investigated. In this condition a baffle (0·05 height, 0·04 breadth) configuration was also studied. The baffle was located in the centre of the tank as shown in Figure 23.

The liquid motion is strongly affected by the geometrical characteristics of the tank. When the unbaffled tank is analysed, the liquid response is similar to that of a slightly damped non linear oscillator. Indeed the small amplitude off-resonance standing waves suddenly change into large

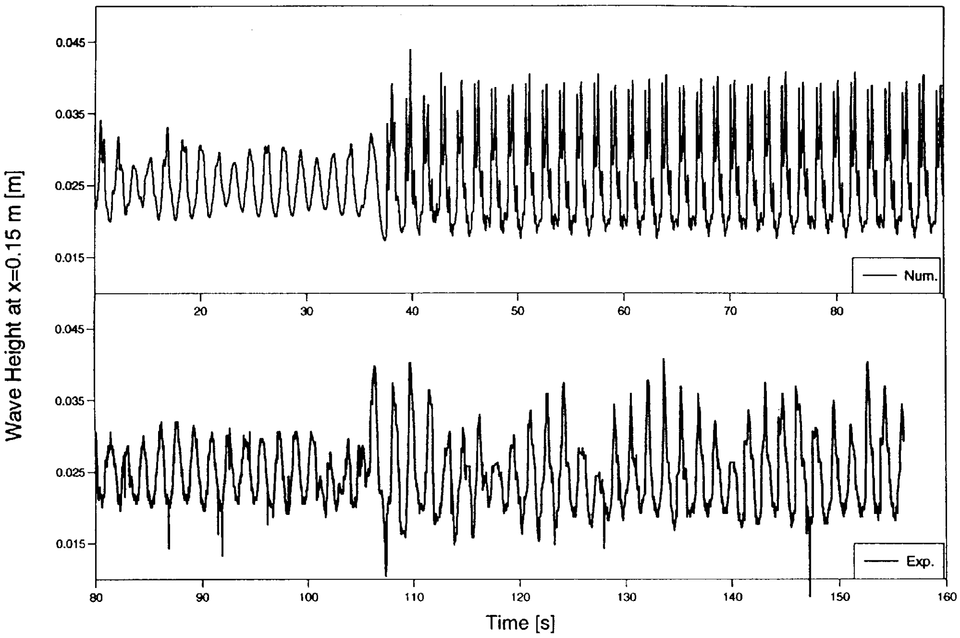

Figure 19. Numerical and experimental time records of wave height at $x = 0{\cdot}15$ m, for $\eta/b = 0{\cdot}05$, $\Omega = 3{\cdot}98$ rad s$^{-1}$ and roll amplitude 0·9°. The presence of two different wave modes (standing wave and hydraulic jump) is shown

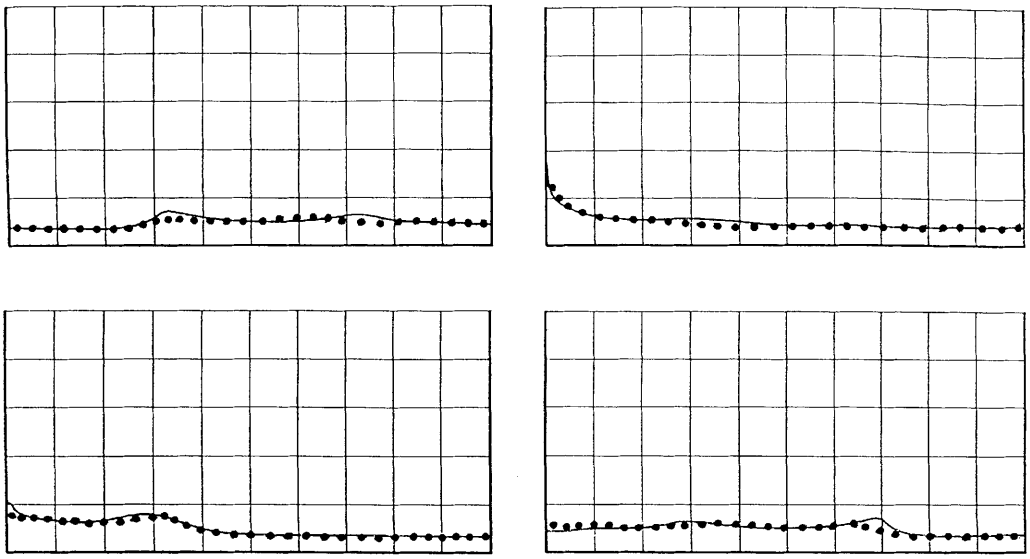

Figure 20. Computed and recorded resonant wave profiles ($\omega = 3{\cdot}47$ rad s$^{-1}$, $\Phi = 0{\cdot}9°$, $\eta/b = 0{\cdot}05$) at four time instants (from top left) $t_1 = 4{\cdot}63$ s, $t_2 = 4{\cdot}93$ s, $t_3 = 5{\cdot}23$ s and $t_4 = 5{\cdot}53$ s

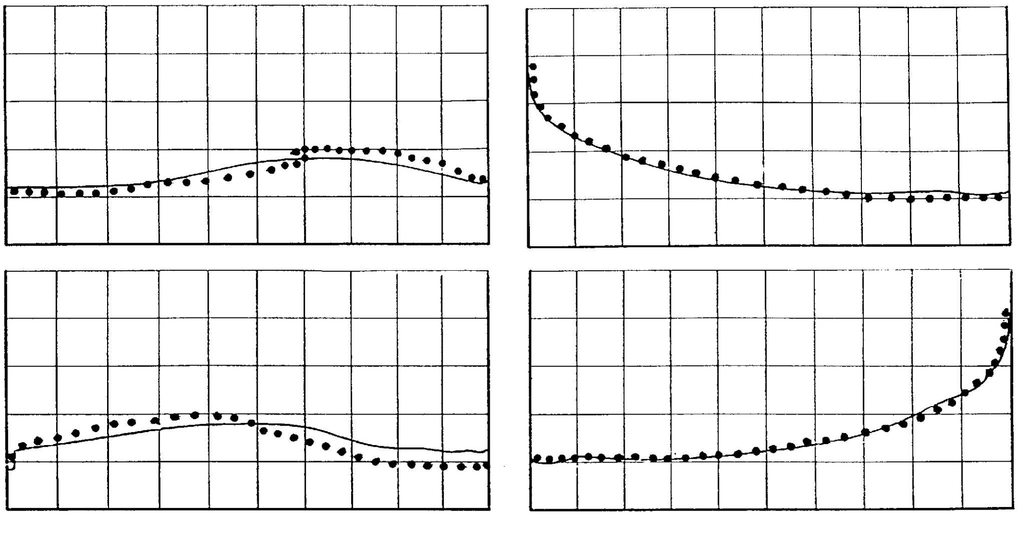

Figure 21. Computed and recorded wave profiles in resonance conditions ($\omega = 5{\cdot}56$ rad s$^{-1}$, $\Phi = 0{\cdot}9°$, $\eta/b = 0{\cdot}05$) at four time instants (from top left) $t_1 = 4{\cdot}25$ s, $t_2 = 4{\cdot}55$ s, $t_3 = 4{\cdot}85$ s and $t_4 = 5{\cdot}15$ s

amplitude waves in a narrow range of frequencies neighbouring the resonant one. The numerical and experimental non-dimensional wave heights at the position of the wave recorder are reported in Figure 24. In this case too the computational results agree fairly well with the experiments. In order to avoid water outflow, the experiments were carried out for the roll amplitude equal to 0·9° in a range of forcing frequencies varying between 3·7 and 5·75 rad s$^{-1}$.

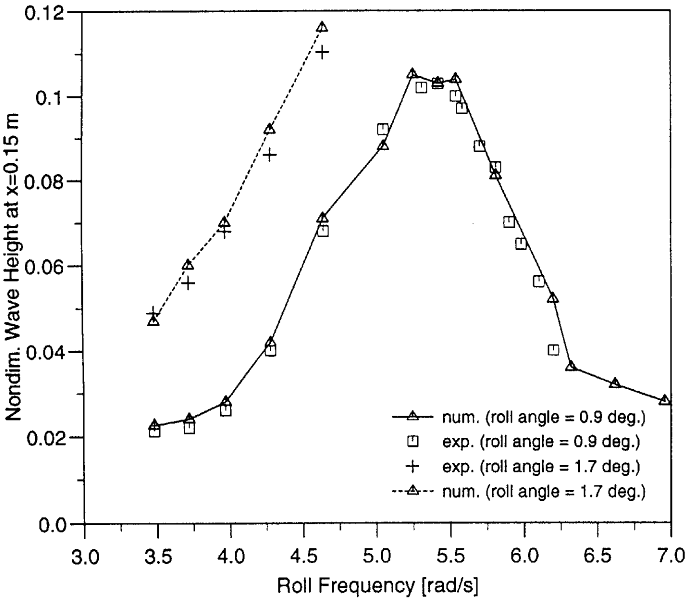

Figure 22. Numerical and experimental non-dimensional wave height at location $x = 0{\cdot}15$ m versus roll frequency for two roll amplitudes ($\eta/b = 0{\cdot}15$)

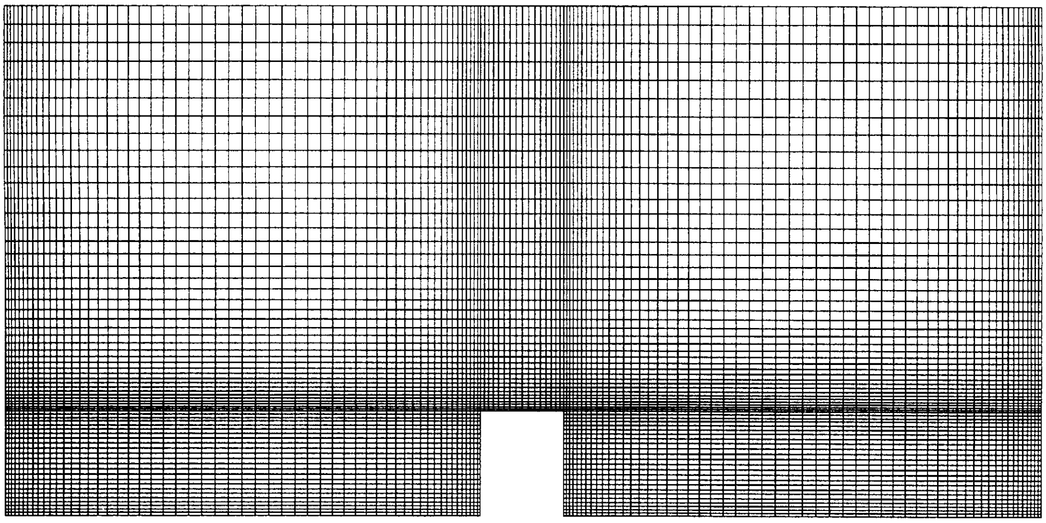

Figure 23. 128 × 64 stretched grid used in computations for baffled geometry

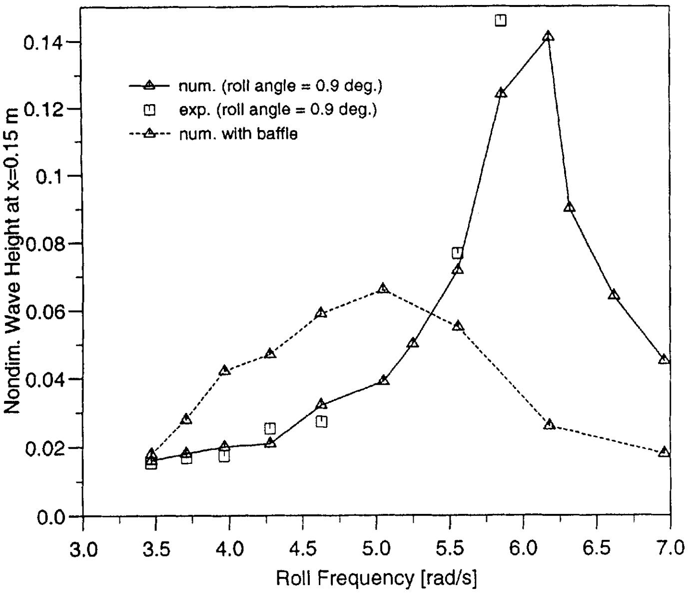

Figure 24. Numerical and experimental non-dimensional wave height at location $x = 0{\cdot}15$ m versus roll frequency for roll amplitude 0·9° and $\eta/b = 0{\cdot}2$ (baffled and unbaffled geometries)

The analysis of the baffled configuration shows very interesting features. The presence of the vertical obstacle causes the generation of large recirculations and a jump-like effect above the obstacle itself (Figure 25). The response in the frequency domain (Figure 24) shows a shift of the resonance frequency from $\Omega = 5{\cdot}76$ to 5·2 rad $s^{-1}$ and a marked reduction of the resonant wave amplitude. According to previous investigations,[25] this effect can be easily explained by the fact that the vertical obstacle inhibits the generation of large amplitude standing waves which turn into small hydraulic jumps owing to shallow water effects over the obstacle.

## 5. CONCLUDING REMARKS

An improved MAC method for the accurate solution of free surface viscous flows has been proposed. The free surface is treated as in a standard MAC method and the fractional step approximate factorization technique for the solution of the Navier–Stokes equations is applied. A multigrid technique based on the additive correction strategy is used in order to speed up the convergence of the pressure equation. As compared with standard methods, the main advantage of the improved MAC method proposed herein lies in the accurate solution of the viscous stress at the solid boundaries. At the same time this method retains the ability of MAC methods to treat distorted free surface patterns such as splashes over rigid walls. Moreover, the use of a multigrid technique for the solution of the pressure equation allows us to solve high-Reynolds flows on an adequately fine stretched grid. As highlighted by several authors, such computations are impracticable if standard MAC methods are applied.

In the first stage of the work grid sensitivity tests were carried out. It was observed that the algorithm can accurately solve the viscous stress at the solid boundaries. In particular streaming layer phenomena were shown in the evolution of the unsteady viscous flow.

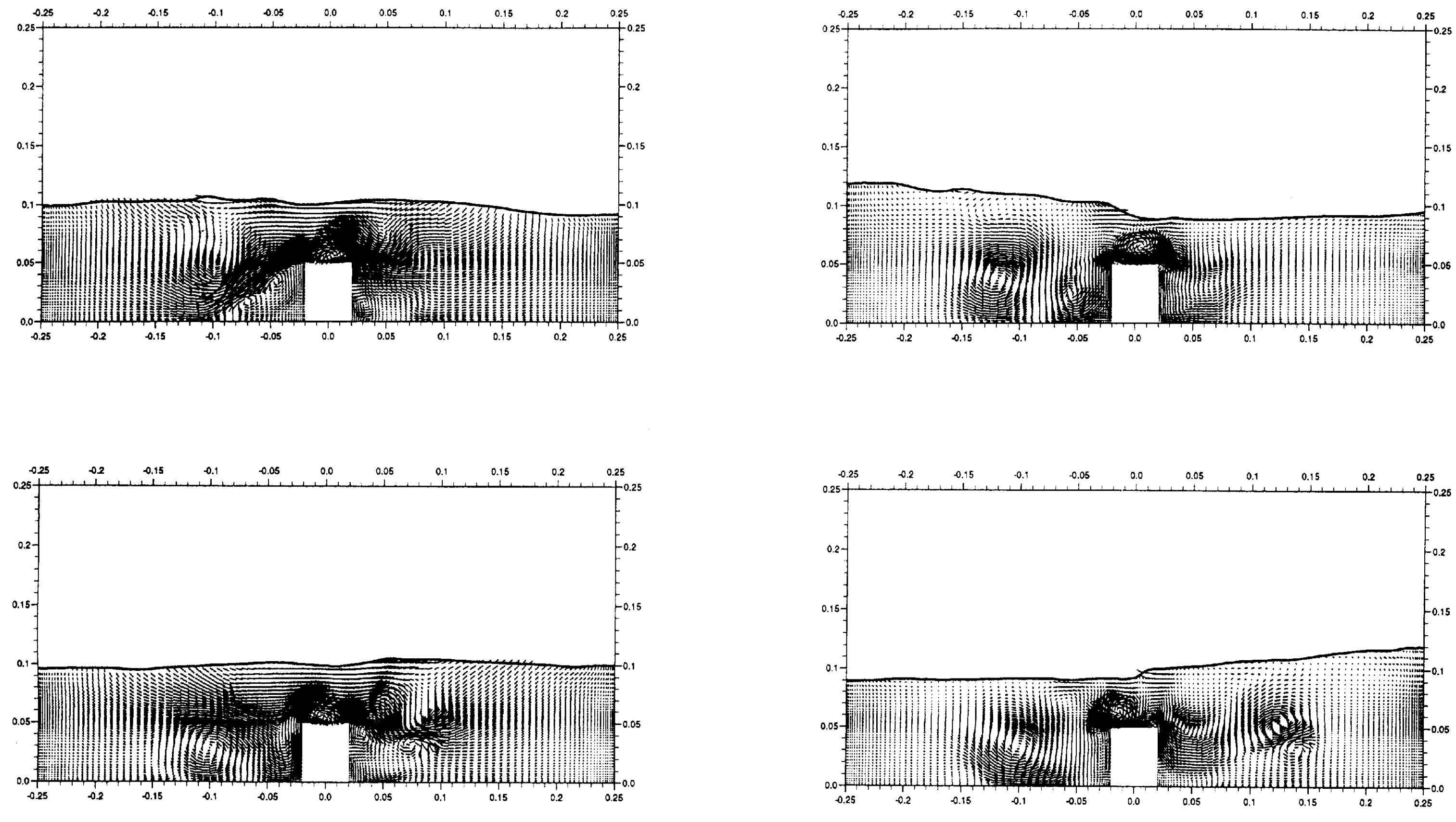

Figure 25. Velocity field in baffled tank at four time instants (from top left) $t_1 = 5{\cdot}41$ s, $t_2 = 5{\cdot}68$ s, $t_3 = 5{\cdot}95$ s and $t_4 = 6{\cdot}22$ s (roll frequency 5·81 rad $s^{-1}$ roll amplitude 0·9°)

The method was then employed for the analysis of water sloshing in rectangular containers. A two dimensional form of the SGS turbulence model was included in the algorithm. In order to validate the numerical results, experimental tests were carried out using a 0·50 m breadth tank partially filled with water.

Computations and experiments were performed for three different filling ratios ranging from shallow water to high depths. The physical features of the phenomenon were accurately predicted by means of the numerical model. In particular, in the shallow water cases, resonant hydraulic jumps appear in a wide range of exciting frequencies and the presence of two different wave modes was experienced in the limiting frequency between the resonance and off-resonance zones.

An increase in the liquid depth inside the tank produces a change in the resonant wave mode from a hydraulic jump to a large travelling wave up to a standing wave. Moreover the increase in the liquid depth causes the resonance zone to be narrowed, since the physical system takes up the characteristics of a slightly damped oscillator system.

In all the cases examined the numerical results agree well with the experiments, both in the prediction of the wave heights and in the description of the wave modes.

Finally, in order to show the effectiveness of the algorithm in simulating free surface high Reynolds flows for a geometry with internal obstacles, computations were also carried out for a rectangular baffled tank.

## ACKNOWLEDGEMENTS

The author gratefully thanks Dr. P. G. Esposito from INSEAN for his suggestions and valuable discussions, and Ing. M. La Rocca from the University of Rome for the experimental tests. The author also has valued comments on the numerical method from Ing. E. Nobile from the University of Trieste.

## REFERENCES

1. J. E. Welch, F. H. Harlow, J. P. Shannon and B. J. Daly, ‘The MAC method’, *Los Alamos Scientific Laboratory Rep. LA-3425*, 1965.
2. R. K. C. Chan and R. L. Street, ‘A computer study of finite-amplitude water waves’, *J. Comput. Phys.*, **6**, 68–94 (1970).
3. B. D. Nichols and C. V. Hirt, ‘Improved free surface boundary conditions for numerical incompressible-flow calculations’, *J. Comput. Phys.*, **8**, 434–448 (1971).
4. J. Viecelli, ‘A computing method for incompressible flows bounded by moving walls’, *J. Comput. Physics*, **8**, 119–143 (1971).
5. B. D. Nichols, C. V. Hirt and R. S. Hotchkiss, ‘SOLA-VOF: a solution algorithm for transient fluid flow with multiple free boundaries’, *Los Alamos Scientific Laboratory Rep. LA–8355*, 1980.
6. H. Miyata and S. Nishimura, ‘Finite difference simulation of nonlinear waves generated by ships of arbitrary three-dimensional configuration’, *J. Comput. Phys.*, **60**, 391–436 (1985).
7. H. Miyata, M. Katsumata, Y. G. Lee and H. Kajitani, ‘A finite difference simulation method for strongly interacting two-layer flow’, *J. Soc. of Naval Archit. Jpn.*, **163**, 1–16 (1988).
8. H. Miyata, ‘Finite difference simulation of breaking waves’, *J. Comput. Phys.*, **65**, 179 –214 (1986).
9. H. Miyata, H. Kajitani, M. Zhu, T. Kawano and M. Takai, ‘Numerical study of some wave-breaking problems by a finite-difference method’, *J. Kansai Soc. Naval Archit.*, **207**, 11–23 (1987).
10. R. W. Yeung and P. Ananthakrishnan, ‘Oscillation of a floating body in a viscous fluid’, *J. Eng. Math.*, **26**, 211–230 (1992).
11. P. Ananthakrishnan and R. W. Yeung, ‘Oscillation of a slightly–submerged cylinder in a viscous fluid’, *Proc. 7th Int. Workshop on Water Waves and Floating Bodies*, Val de Ruil, 5–9 (1992).
12. J. P. V. Cordonnier, ‘Numerical simulation of sloshing in tanks’, in T. K. S. Murthy and P. A. Wilson (eds), *Marine, Offshore and Ice Technology*, Computational Mechanics Publications/Wadhams, Boston, MA, 1994, pp. 197–204.
13. P. M. Gresho, ‘On the theory of semi–implicit projection methods for viscous incompressible flow and its implementation via a finite element method that also introduces a nearly consistent mass matrix. Part 1: Theory’, *Int. j. numer. methods fluids*, **11**, 587–620 (1990).
14. J. Kim and P. Moin, ‘Application of a fractional step to incompressible Navier–Stokes equations’, *J. Comput. Phys.*, **59**, 308–323 (1985).

15. P. G. Esposito, ‘Numerical simulation of 3–D incompressible unsteady viscous laminar flows’, *Notes Numer. Fluid Mech.*, **36**, 46–52 (1992).
16. A. Huser and S. Biringen, ‘Calculation of two–dimensional shear-driven cavity flow at high Reynolds numbers’, *Int. j. num. methods fluids*, **14**, 1087–1109 (1992).
17. J. Zhu, ‘On the higher–order bounded discretisation schemes for finite volume computations of incompressible flows’, *Comput. Methods Appl. Mech. Eng.*, **98**, 345–360 (1992).
18. B. R. Hutchinson and G. D. Raithby, ‘A multigrid method based on the additive correction strategy’, *Num. Heat Transfer*, **9**, 511–537 (1986).
19. D. P. Telionis, *Unsteady Viscous Flows*, Springer, New York, 1980.
20. T. Eguchi and O. Niho, ‘A numerical and experimental study of sloshing problems’, *Hydrosoft*, **2**, 27–36 (1989).
21. S. Tozawa and H. Sueoka, ‘Experimental and numerical studies on sloshing in partially filled tank’, *Proc. PRADS’89*, Varna, 1989, Vol. 2, pp. 57.1–57.8.
22. H. A. Olsen and T. Hysing, ‘A study of dynamic loads caused by liquid sloshing in LNG tanks’, *Rep. 74–276–C*, Maritime Administration, Det Norske Veritas, 1974.
23. Y. K. Lou, T. C. Su and J. E. Flipse, ‘A nonlinear analysis of liquid sloshing in rigid containers’, *Texas A, 1980.*
24. J. R. Ockendon and H. Ockendon, ‘Resonant surface waves’, *J. Fluid Mech.*, **59**, 397-413 (1973).
25. T. C. Su, J. K. Lou, J. E. Flipse and T. J. Bridges, ‘A numerical analysis of large amplitude liquid sloshing in baffled container’, *Texas A&M University College Station Rep. MA-RD-940-82046*, 1982.